Title

Formation of hydrided Pt-Ce-H sites in efficient, selective oxidation catalysts

Authors

Yang, Ji
Falling, Lorenz J
Yan, Siyang
et al.

Publication Date

2025-04-03

DOI

10.1126/science.adv0735

Title: Formation of hydrided Pt-Ce-H sites in efficient, selective oxidation catalysts

Authors: Ji Yang[1]†, Lorenz J. Falling[2]†, Siyang Yan[3]†, Biluan Zhang[4]†, Pragya Verma[5]†, Luke Daemen[6], Yongqiang Cheng[6], Xiao Zhao[7], Shuchen Zhang[7], Jeng-Lung Chen[8], Bingqing Yao[9], Shengdong Tan[9], Sudong Chae[1], Qian He[9], Slavomir Nemsak[2], Zili Wu[10], David Prendergast[5]*, Yanbing Guo[4]*, Jiaxu Liu[3]*, Miquel Salmeron[7,11]*, Ji Su[1]*

Affiliations:

[1]Energy Storage and Distributed Resources Division, Lawrence Berkeley National Laboratory; Berkeley, California 94720, United States.

[2]Advanced Light Source, Lawrence Berkeley National Laboratory; Berkeley, California 94720, United States.

[3]Department of Catalytic Chemistry and Engineering, Dalian University of Technology; Dalian 116024, China.

[4]College of Chemistry, Central China Normal University; Wuhan 430079, China.

[5]The Molecular Foundry, Lawrence Berkeley National Laboratory; Berkeley, California 94720, United States.

[6]Neutron Scattering Division, Oak Ridge National Laboratory; Oak Ridge, Tennessee 37831, United States.

[7]Materials Sciences Division, Lawrence Berkeley National Laboratory; Berkeley, California 94720, United States.

[8]National Synchrotron Radiation Research Center, Science-Based Industrial Park; Hsinchu 300092, Taiwan.

[9]Department of Materials Science and Engineering, National University of Singapore; Singapore 117575, Singapore.

[10]Chemical Sciences Division, Oak Ridge National Laboratory; Oak Ridge, Tennessee 37831, United States.

[11]Department of Materials Science and Engineering, University of California, Berkeley; Berkeley, California 94720, United States.

†These authors contributed equally to this work.

*Corresponding authors. Email: jisu@lbl.gov; mbsalmeron@lbl.gov; liujiaxu@dlut.edu.cn; guoyanbing@mail.ccnu.edu.cn; dgprendergast@lbl.gov

Abstract: Single-atom site catalysts can improve the rates and selectivity of many catalytic reactions. We have modified Pt_1/CeO_2 single sites by combining them with molecular groups and with oxygen vacancies of the support. The new sites include hydrided (Pt^{2+}-$Ce^{3+}H^{\delta-}$) and hydroxylated (Pt^{2+}-$Ce^{3+}OH$) sites that exhibit higher reactivity and selectivity to previous single sites for several reactions, including a ninefold increase in the reaction rate for carbon monoxide (CO) oxidation, and a 2.3-fold improvement of propylene selectivity for oxidative dehydrogenation of propane. The atomic structure and reaction steps of these sites were determined with in situ and ex situ spectroscopy techniques and theoretical methods.

Main Text:

Supported metal catalysts have widespread applications in the chemical industry and environmental cleaning (*1–5*). Metal–support interactions (MSIs) are usually exploited to modulate catalyst activity (*6–10*). Typical MSI effects can lead to metal-support charge transfer, restructuring of metal nanoparticles (NPs), and chemical composition exchange, which provide synergistic properties to control catalysis (*6*, *11*). Generally, the efficiency of MSI reactivity enhancement decays rapidly with increasing metal NPs size, with the highest enhancements found in NPs <4 nm in diameter. For single metal atoms, the interaction with the support is amplified by the increased number of metal-support bonds (*6*, *12–14*).

Single metal atoms can pair with neighboring metal atoms and oxygen vacancies (V_o) sites under MSI effects (*13*, *15*) to form a colocalized active site with synergies that have been shown to attain improved performance for heterogeneous catalysis. For example, co-localized active sites have been reported to facilitate desirable elementary steps, where the new activation mechanisms provide higher reaction rates and selectivity (*16*)(*17*). Further, the synergy between single Pt atoms and the CeO_2 support and with V_o sites, can efficiently help dehydrogenation of large molecular cyclohexane to benzene, outperforming traditional Pt NP catalysts (*13*). Recent studies indicate that the single-atom MSIs have a differentiated state and can be fine-tuned by the size of support (*18*).

These findings motivated our study of co-localization, geometry, oxidation states, and new interactions of the constituent atoms and functional groups in adjacent sites. We show that starting with Pt_1/CeO_2 single sites, we can create new hydrided sites Pt^{2+}-$Ce^{3+}H^{\delta-}$, as well as hydroxylated Pt^{2+}-$Ce^{3+}OH$ pairs that, compared to the original Pt_1/CeO_2 single sites, exhibit higher CO oxidation activity by a factor of 9. The active Ce-H hydride and Ce-OH hydroxide species formed only at Pt^{2+}-Ce^{3+} pair sites on the CeO_2 support with proper reduction.

To determine the atomic structure and chemical reactions forming these new sites and their interaction with reactant species, we used an array of in situ and ex-situ spectroscopies and theoretical calculations. The critical role of the $H^{\delta-}$ catalytic site in enhanced O_2 activation and catalytic performance is highlighted. Our work demonstrates an easy but overlooked approach to tailoring the catalytic properties of single-atom site catalysts by hydrogenation of active sites. The concept of hydrided sites can be extended to supported metal NP catalysts (*19–23*) for many reactions, such as methanol synthesis by CO_2 hydrogenation, and others, warranting further study to understand the effects and promises of hydrided sites (with their broader implications detailed in the Supplementary Material).

Active-site formation

We prepared single Pt atoms on CeO_2 nanopowder (Pt_1/CeO_2) with a particle sizes < 20 nm using wet-synthesis method. Typically, the H_2PtCl_6 precursor was hydroxylated to $[PtCl_4(OH)_2]^{2-}$ in a weakly basic solution (pH =8) (*24*), and the CeO_2 surface became positively charged as its isoelectric pH value is ~ 8.7 (see fig. S1) (*25*, *26*). The strong electrostatic adsorption promoted repulsive interactions between Pt ions in solution, which distributed isolated Pt ions on CeO_2 surface. Further vacuum drying at 200°C helped eliminate solution residues to obtain Pt_1/CeO_2 (fig. S2), which after H_2 reduction at 200°C enabled integration of the Pt atoms to generate the hydrided-site catalyst.

The interaction between the Pt atoms and CeO_2 matrix during reduction was monitored by the evolution of the Pt 4*f* and Ce 4*d* ambient-pressure x-ray photoelectron spectroscopy (AP-XPS) peaks in 100 mTorr H_2 at increasing temperatures (Fig. 1**A**). Before H_2 reduction, the Pt 4*f 7/2* binding energy was 76 eV, which compares well with that of octahedrally coordinated Pt^{4+} in PtO_2 and K_2PtCl_6 (*27*). Cerium in the Ce^{4+} state contributed peaks at 123 and 126 eV, whereas mixed Ce^{3+} and Ce^{4+} contributed peaks between 108 and 120 eV (*28*). Using principal component analysis, we deconvoluted the Ce 4*d* features to quantify the change in oxidation state in a series of Ce 4*d* spectra at temperatures steps from ~60° to ~390°C. As temperature increased from ~60° to 250°C, Pt^{4+} and Ce^{4+} were gradually reduced, as evidenced by a growing Pt 4*f* doublet with a 7/2 line at lower binding energy of 75 eV, and a larger relative contribution of Ce^{3+} between 108 and 120 eV, as well as 107 eV, where Ce^{4+} does not contribute (*28*).

The reduction rate of Pt (Fig. 1**A**, center panel) was faster > 250°C and reached a plateau at 310°C with ~10% of Pt^{4+} remaining. Although the reduction to metallic Pt could be excluded as shown by the binding energy and symmetric line shape of the Pt 4*f* XPS peak, the final oxidation state remains could not be determined from XPS data alone. A more direct measure of the electron and hole density was obtained from x-ray absorption near-edge structure (XANES) analyses (fig. S3), which indicated that the a Pt oxidation state between +4 and +2 for atomic Pt on CeO_2 nanopowder after H_2 reduction (we denoted the sample after reduction as Pt_1-Ce/CeO_{2-x}) (*29*).

The Pt 4*f* doublet at 75 eV therefore related to Pt^{2+}. The CeO_2 support reduction was not as rapid, and had an onset at ~150°C. The contribution of Ce^{3+} to the XPS peak continued to grow, reaching ~40% at ~390°C, which was ~10% higher than that for the reference CeO_2 sample without Pt. The generation of Ce^{3+} species on Pt_1-Ce/CeO_{2-x} by reduction in H_2 was also confirmed by in-situ electron energy loss spectroscopy (EELS) results (figs. S4 and table S1) (*30*). These findings suggested that atomic Pt facilitated the reduction of CeO_2 through H atom spillover effect (see Supplementary Material for a discussion on the ability of ionic Pt sites to dissociate H_2).

Local structure of hydrided sites

Fourier-transform of extended x-ray absorption fine structure (FT-EXAFS) spectra revealed the atomic dispersion of Pt sites for Pt_1/CeO_2 single sites and Pt_1-Ce/CeO_{2-x} (Fig. 1**B**), as indicated by the absence of Pt-Pt scattering peak. The strong stabilization of single Pt atoms on CeO_2 was also corroborated by the identification of Pt-O and Pt-O-Ce coordination shells in two samples (Fig. 1**B**). Additionally, high-resolution high-angle annular dark-field scanning transmission electron microscopy (HAADF-STEM) images, and intensity line profiles (fig. S5), confirmed the single-atom state of Pt sites on CeO_2 (see the Supplementary Material for a detailed feasibility analysis of statistical analysis in HAADF-STEM imaging). EXAFS curve-fitting results (fig. S6 and table S2) showed that Pt-O coordination numbers (CN) for Pt_1/CeO_2 and Pt_1-Ce/CeO_{2-x} were 5.9 and 4.2, respectively.

Because of the high sensitivity of the C-O bond stretch mode to the local electronic structure of the adsorption site, we used CO as a probe molecule to characterize the outermost atomic structure of the catalysts. Fourier-transform infrared (FTIR) spectra taken after CO adsorption at 77 K revealed the presence of different Ce and Pt sites (Fig. 1**C**) corresponding to Pt_1/CeO_2, Pt_1-Ce/CeO_{2-x}, and CeO_{2-x} control samples. Six distinct peaks at 2170, 2156, 2129, and 2106/2104/2087 cm^{-1} were assigned to CO adsorption on Ce^{3+}, Ce^{4+}, CO physisorption on ionic $Pt^{\delta+}$, and chemisorption (*CO) on ionic $Pt^{\delta+}$, respectively, with different local structures (*14*). The CO adsorption peak on Ce^{3+}, centered at 2170 cm^{-1} in Pt_1-Ce/CeO_{2-x}, was blue-shifted to 2178 cm^{-}

^{1} on pure CeO_{2-x} samples, whereas the peak position of CO absorbed on Ce^{4+} remained unchanged. This difference strongly indicated that the Ce^{3+} created in Pt_1-Ce/CeO_{2-x} was chemically different from that in reduced CeO_{2-x}. The lower wavenumber of the CO peak on Ce^{3+} in Pt_1-Ce/CeO_{2-x} revealed the spatial proximity and electronic interaction between Ce^{3+} and Pt^{2+}.

We also performed in-situ inelastic neutron scattering (INS) studies to determine the speciation of H atoms during spillover (Fig. 1**D**). The strong shoulder peaks at 399 and 465 cm^{-1} and a broad peak at 859 cm^{-1} are observed with the reduction by H_2 we attributed to Ce-H hydrides on the surface and in the bulk, respectively (*31*). The spectral features remained unchanged after further 120°C-vacuum treatment, indicating that surface Ce-H and bulk Ce-H hydrides were stable, and excluded the possibility of surface species such as adsorbed water.

Density functional theory (DFT) calculations were performed to further understand the electronic and geometric structure change of surface sites during H_2 reduction. APXPS, x-ray diffraction (XRD), and EXAFS results (Fig. 1**A**, fig. S7, and table S2) indicated octahedrally O-coordinated Pt^{4+} in Pt_1/CeO_2 on the CeO_2 (111) surface, which was used as the starting point in DFT calculations (left panel in Fig. 1**E**, fig. S8). We associated the H_2 reduction process with the creation of oxygen vacancies (Vo). Combined with the above spectroscopic results, our theoretical results (figs. S8 to S11 and table S3) showed that the generation of Vo sites created Pt^{2+}-Ce^{3+} pair sites, with an increased population of adjacent Ce^{3+} created by H from spillover effects (See detailed analysis in fig. S7).

Moreover, we found that the active Ce-H hydrided sites could be formed only at Pt^{2+}-Ce^{3+} pair sites with more than three nearby Vo sites that created an electron-rich surface site. Fig. 1**E** (right panel) shows the formation of 2 Ce-H hydrides (Ce-$H^{\delta-}$) on Pt_1-Ce/CeO_{2-x}_3Vo model after H_2 activation. Bader charge analysis indicated that each H atom gained 0.6 e^- from adjacent Ce^{3+} to form the hydride. On the Pt_1-Ce/CeO_{2-x}_6Vo model surface that had a higher surface electron density than Pt_1-Ce/CeO_{2-x}_3Vo (fig. S12 and table S3), two Ce-$H^{\delta-}$ are also formed with favorable thermodynamics (fig. S12). However, only two lattice OH groups were formed on Pt_1/CeO_2 and Pt_1-Ce/CeO_{2-x}_1Vo models by bonding with lattice oxygen after H_2 dissociation (fig. S13). Even on Pt_1-Ce/CeO_{2-x}_2Vo model, only one proton (donating 0.5 e^-) and one $H^{\delta-}$ (gaining 0.2e^-) at Pt^{2+} could be formed (fig. S14 and table S3). These findings supported the formation of hydrided sites Pt^{2+}-Ce^{3+}($H^{\delta-}$) on Pt_1-Ce/CeO_{2-x} nanopowder after H_2 reduction and suggested the importance of retaining electron-enriched surface states to create hydrided sites.

Hydrided-site enhanced surface reactivity

We used CO oxidation to probe the activity of hydrided sites Pt^{2+}-Ce^{3+}($H^{\delta-}$) (Fig. 2, **A** to **C**, and figures S15 to S18). The introduction of Pt atoms on CeO_2 increased the CO oxidation activity (fig. S15). In particular, the temperature at 10% CO conversion (T_{10}) on Pt^{2+}-Ce^{3+}($H^{\delta-}$) hydrided sites in the first run was 40°C lower than in the second and third runs (80 °C versus 120 °C, Fig. 2**A**). This result showed that hydrided sites improved substantially surface reactivity, whereas the active species were likely consumed rather than replenished. However, after 3% H_2 addition, T_{10} could be sustained and CO conversion at 160°C was increased from 33.8% to 100% on Pt^{2+}-Ce^{3+}($H^{\delta-}$) hydrided sites within three runs (Fig. 2**A**). Fig. 2**B** shows that the turnover frequency (TOF) of CO, O_2, and H_2 at 100°C on Pt^{2+}-Ce^{3+}($H^{\delta-}$) hydrided sites was ~9, ~29, and ~135-fold higher, respectively, than on Pt_1 single sites, indicating a higher and more effective activation of CO, O_2, and H_2. This result was consistent with the favorable kinetics of CO activation by Pt^{2+}-Ce^{3+}($H^{\delta-}$) hydrided sites (fig. S16).

To study the properties of Pt^{2+}-Ce^{3+}($H^{\delta-}$) hydrided sites, we compared CO oxidation performance of the catalyst in the presence of H_2 in different conditions. We found that Pt^{2+}-Ce^{3+}($H^{\delta-}$) hydrided sites could be passivated in oxidative environment (fig. S17). Time-on-stream CO oxidation tests indicated that CO conversion on Pt^{2+}-Ce^{3+}($H^{\delta-}$) hydrided sites decreased from 13.6% to 3.3% within 1.5 h in the absence of H_2 co-feeding (fig. S17), and then remained unchanged. A constant feed of 3% H_2 sustained the CO conversion at ~13.0% for > 4h. This process was also reversible (Fig. 2**C**). By contrast, Pt single sites displayed approximately constant CO conversion of <2% with and without H_2 co-feeding (fig. S18). These results highlighted the high sensitivity of Pt^{2+}-Ce^{3+}($H^{\delta-}$) hydrided sites to H_2 and demonstrate their sustained high surface reactivity in a H_2-containing environment.

We then used the hydrided-site catalyst for CO preferential oxidation (PROX), a promising H_2 purification process providing high-purity H_2 for proton-exchange membrane fuel cells (*32*, *33*). As shown in Fig. 3**A**, O_2-to-CO_2 selectivity for Pt^{2+}-Ce^{3+}($H^{\delta-}$) hydrided-site catalyst could reach 85.5% at 80°C at a CO conversion of 16.9%. The limited CO conversion is the result of insufficient Pt sites [Pt weight loading of 0.044% as determined by inductively coupled plasma-optical emission spectroscopy (ICP-OES), shown in table S4]. When the Pt weight loading of hydrided-site catalyst was increased to 0.15% (table S5), CO conversion reached >99.9% at 80°C after 24h with a weight hourly space velocity (WHSV) of 12000 mL g^{-1} h^{-1} (Fig. 3**B**). The high stability of the hydrided sites for CO PROX was further demonstrated by maintaining ~61% CO conversion over 24 hours at an increased WHSV (Fig. S19). The advantages of hydrided-site catalysts in CO PROX reaction compared to other state-of-the-art catalysts (table S6) are detailed in the Supplementary Material. In addition, the hydrided sites exhibited enhanced propane conversion and markedly higher selectivity for oxidative dehydrogenation of propane (ODP), with the propylene (C_3H_6) selectivity increased by 2.3 times compared to that of Pt single sites (Fig. 3, **C** and **D**). Moreover, the Pt sites in hydrided-site catalyst with 0.15% Pt loading maintained atomic dispersion after undergoing CO PROX reaction, or ODP reaction (see HAADF-STEM analysis results in fig. S20 and S21). A comprehensive discussion on the good thermal stability (fig. S22) of the hydrided-site catalyst is provided in the Supplementary Material. These results indicated that the formation of hydrided sites offers new capabilities for catalyzing other important reactions.

We used INS spectra to study hydride speciation under low-temperature CO oxidation conditions, (Fig. 2**D**). When Pt^{2+}-Ce^{3+}($H^{\delta-}$) hydrided sites were exposed to an O_2 atmosphere the features of Ce-H hydrides (399, 465, and 859 cm^{-1}, Fig. 1**D**) diminished, and a new band appeared, centered at 589 cm^{-1} (Fig. 2**D**), that we assigned to hydroxyl groups (OH) through the reaction between Ce-H hydrides and molecular O_2. CO purge generated a broad and intensive band at 578 cm^{-1}, which was caused by water formation generated from $CO + 2OH \rightarrow CO_2 + H_2O$.

In-situ FTIR studies were used to determine O_2 speciation (Fig. 2**E**). Pt_1 single sites (in vacuum) exhibited two different types of OH adsorption that we identified as isolated OH at Ce^{4+} (3703 cm^{-1}) and bridging OH (3646 cm^{-1}) (*31*, *34*, *35*). Subsequent H_2 reductive treatment was applied to in-situ generate Pt^{2+}-Ce^{3+}($H^{\delta-}$) hydrided sites, where the peak intensity of the OH decreased through reaction with dissociated H species to form water (*31*). O_2 feeding generated a new band at 3684 cm^{-1} associated with OH bonded at Ce^{3+} (*31*, *36*), whereas isolated and bridging OH peaks remained unchanged. When purging with CO, only the peak of OH on Ce^{3+} at 3684 cm^{-1} disappeared (inset in Fig. 2**E**), indicating its consumption by CO oxidation and its high reactivity. The products CO_2 and H_2O were detected by mass spectrometry (fig. S23), confirming our conjecture in the INS analysis that H_2O was generated by reaction of CO with reactive OH.

DFT calculations provided further insight into hydrided-site controlled O_2 activation. When O_2 was introduced, two OH groups formed on Ce^{3+} (Ce^{3+}-OH) (Fig. 2**F**). The calculated stretching vibration frequencies of these OH groups was 3684 and 3643 cm^{-1}, in line with our FTIR observations (Fig. 2**E**). When generating more Vo sites (e.g. 6Vo) around Pt^{2+}-Ce^{3+}($H^{\delta-}$) hydrided sites, Ce^{3+}-OH species were also readily formed after arrival and dissociation of O_2 (fig. S24). However, molecular O_2 adsorption and activation preferentially occur at unoccupied Vo sites if hydrided sites were not well formed on electron-deficient surface sites (fig. S25 and table S3). Our findings indicated that the formation of hydrided sites Pt^{2+}-Ce^{3+}($H^{\delta-}$) was critical to regulating the O_2 activation pathway.

Hydride-Transfer Catalysis Mechanism

We developed a hydrided-site synergistic mechanism for CO oxidation using DFT calculations (Fig. 4, figs. S26 to S32, and data S1 to S11), with computational methods detailed in Supplementary Material. Fig. 4**A** and fig. S26 show four pathways for the formation of hydrided sites Pt^{2+}-Ce^{3+}($H^{\delta-}$) from H_2 dissociation at Pt sites and subsequent spillover to Ce^{3+} and forming the active Ce-H hydrided site. Depending on the H spillover path, the final structure of the hydride will determine the energy barrier (E_a) for H_2 activation, varying from 0.13 to 0.16 eV (Fig. 4**B**). The final Pt^{2+}-Ce^{3+} ($H^{\delta-}$) sites serve as highly reactive catalytic sites for CO oxidation (Fig. 4**C**). The key role of Pt (fig. S27) in forming hydrided sites is detailed in Supplementary Material. Our DFT calculation results show that the hydrides ($H^{\delta-}$) could be recycled or consumed in each CO oxidation cycle.

In the $H^{\delta-}$ recycling path (upper diagram in Fig. 4**C**), both two $Ce^{3+}H^{\delta-}$ sites are adjacent to Pt atoms within its first and second coordination sphere (generated from H spillover path I and II), which activate adsorbed molecular O_2 ([1]) to form two reactive OH ([2]) at the same Ce^{3+} (Ce^{3+}-OH) after overcoming an E_a of 0.29 eV ([TS1]). Once CO is adsorbed at Pt site ([3]), CO oxidation readily proceeds through the coupling of CO and Ce^{3+}-OH to yield carboxyl (*COOH, [TS2]), which is then decomposed to generate the first CO_2 and return the $H^{\delta-}$ ([4]). This is the rate-determining step (RDS) with an activation energy Ea of 0.43 eV ([TS2]). The other Ce^{3+}-OH reacts with another adsorbed CO at the Pt site and undergoes a similar oxidation process ([5]), with an Ea of 0.42 eV ([TS3]). After releasing the second CO_2 and restoring the second $H^{\delta-}$ ([FS]), hydrided-sites Pt^{2+}-Ce^{3+} ($H^{\delta-}$) are recovered for the next catalytic cycle.

The pathway and energy of O_2 activation in the $H^{\delta-}$ consumption path (lower diagram in Fig. 4**C**) is similar to that in the $H^{\delta-}$ recycling path, with the difference that (i) one of the $Ce^{3+}H^{\delta-}$ sites, and the subsequently created Ce^{3+}-OH site, is located beyond the second coordination sphere of Pt site (represented by H spillover path III and IV) and (ii) the generated *COOH (by overcoming Ea of 0.35 eV) tends to react with the other Ce^{3+}-OH to release CO_2 and H_2O because of their spatial proximity, which is the RDS with an Ea of 0.42 eV.

We found that two $H^{\delta-}$ transfer pathways for CO oxidation displayed comparable energy barriers for the RDS (0.43 vs 0.42 eV). Considering the molar balance of elements in a catalytic reaction, the $H^{\delta-}$ recycling and consumption path for CO oxidation has O_2-to-CO_2 selectivity of 100% and 50%, respectively. Our CO PROX results (Fig. 3**A**) showed that Pt^{2+}-Ce^{3+}($H^{\delta-}$) hydrided-site catalyst displayed a O_2-to-CO_2 selectivity of >50% below 120 °C, which indicated that both $H^{\delta-}$ recycling and consumption paths were involved in the CO oxidation process. Further DFT calculations revealed that two CO oxidation pathways showed decreasing Ea for the RDS with the increase of surface Vo coverage (fig. S28). In particular, creating a highly electron-rich surface (i.e., more reduced sites) enabled the $H^{\delta-}$ recycling with more favorable kinetics than in the $H^{\delta-}$ consumption path (for example, with 9 Vo, Ea was 0.40 versus 0.43 eV with 9 Vo). These findings demonstrate the strong impact of the (atomic and electronic) structure of hydrided sites Pt^{2+}-Ce^{3+}($H^{\delta-}$) on the CO oxidation mechanism.

In contrast to the high reactivity of Ce^{3+}-OH formed on Pt^{2+}-Ce^{3+}($H^{\delta-}$), the lattice OH groups on the Pt_1 single-site model, formed by the reaction of dissociated H with lattice O, were inactive for CO oxidation (fig. S29). This reaction proceeds through the Mars-van-Krevelen (Mvk) mechanism on Pt_1/CeO_2 (fig. S30), where CO was oxidized by surface lattice oxygen (as RDS) with an E_a of 0.70 eV. Theoretical calculations showed that the CO oxidation pathway shifted from MvK mechanism (0.77 eV) on Pt single sites to a kinetically favorable Langmuir–Hinshelwood (L-H) mechanism (0.52 eV) on Pt^{2+}-Ce^{3+} sites in the absence of H_2 (figs. S31 and S32). However, their RDS are restricted by the low reactivity of lattice and adsorbed oxygen and sluggish O abstraction by *CO.

Comparatively, with the formation of Pt^{2+}-Ce^{3+}($H^{\delta-}$) hydrided sites, the O_2 activation pathway was fundamentally changed, and CO could be readily oxidized to CO_2 by $Ce^{3+}H^{\delta-}$ site-activated Ce^{3+}-OH with a low RDS barrier of ~0.40 eV. This marked decrease of RDS energy barrier explained the excellent CO oxidation activity of Pt^{2+}-Ce^{3+}($H^{\delta-}$) hydrided-site catalyst at low temperatures (Fig. 2, **A** and **B**). Moreover, CO oxidation proceeded through the $H^{\delta-}$ recycling path when two $Ce^{3+}H^{\delta-}$ sites were within the first and second coordination sphere of Pt^{2+}, which shifted to a $H^{\delta-}$ consumption path if $H^{\delta-}$ spills over to a more distant Ce^{3+} site. Our DFT results demonstrate the advantage of Pt^{2+}-Ce^{3+} ($H^{\delta-}$) hydrided sites in CO oxidation and underscore the critical role of proximal atom synergy in multi sites to accelerate catalytic reactions. Further, the $H^{\delta-}$ transfer mechanism provides new insights into the role of the $H^{\delta-}$ site in oxidation reactions.

Summary

We demonstrated the formation of Pt^{2+}-Ce^{3+}($H^{\delta-}$) hydrided sites by modification of Pt single-atom sites on CeO_2 with a reaction rate nine times higher for CO oxidation than that of Pt single sites. With the help of APXPS, XANES, EELS, FTIR, INS characterization, and DFT simulations, we determined the structure and formation mechanism of the new Pt^{2+}-Ce^{3+}($H^{\delta-}$) hydride sites, and CO oxidation mechanism. Our study offers new opportunities for catalyst innovations and new breakthroughs in industrial reactions such as the selective oxidation of short-chain alkanes.

References and Notes

1. Y. Guo, M. Wang, Q. Zhu, D. Xiao, D. Ma, Ensemble effect for single-atom, small cluster and nanoparticle catalysts. *Nat. Catal.* **5**, 766–776 (2022).

2. C. Vogt, B. M. Weckhuysen, The concept of active site in heterogeneous catalysis. *Nat. Rev. Chem.* **6**, 89–111 (2022).

3. L. Liu, A. Corma, Metal catalysts for heterogeneous catalysis: From single atoms to nanoclusters and nanoparticles. *Chem. Rev.* **118**, 4981–5079 (2018).

4. P. Munnik, P. E. de Jongh, K. P. de Jong, Recent developments in the synthesis of supported catalysts. *Chem. Rev.* **115**, 6687–6718 (2015).

5. S. Mitchell, J. Pérez-Ramírez, Atomically precise control in the design of low-nuclearity supported metal catalysts. *Nat. Rev. Mater.* **6**, 969–985 (2021).

6. T. W. Van Deelen, C. Hernández Mejía, K. P. de Jong, Control of metal-support interactions in heterogeneous catalysts to enhance activity and selectivity. *Nat. Catal.* **2**, 955–970 (2019).

7. S. J. Tauster, S. C. Fung, R. T. K. Baker, J. A. Horsley, Strong interactions in supported-metal catalysts. *Science* **211**, 1121–1125 (1981).

8. S. J. Tauster, S. C. Fung, Strong metal-support interactions: Occurrence among the binary oxides of groups IIA-VB. *J. Catal.* **55**, 29–35 (1978).

9. F. Tao, M. Salmeron, Surface restructuring and predictive design of heterogeneous catalysts. *Science* **386**, eadq0102 (2024).

10. T. Wang, J. Hu, R. Ouyang, Y. Wang, Y. Huang, S. Hu, W. Li, Nature of metal-support interaction for metal catalysts on oxide supports. *Science* **386**, 915–920 (2024).

11. P. Wu, S. Tan, J. Moon, Z. Yan, V. Fung, N. Li, S. Z. Yang, Y. Cheng, C. W. Abney, Z. Wu, A. Savara, A. M. Momen, D. en Jiang, D. Su, H. Li, W. Zhu, S. Dai, H. Zhu, Harnessing strong metal–support interactions via a reverse route. *Nat. Commun.* **11**, 3042 (2020).

12. L. N. Chen, K. P. Hou, Y. S. Liu, Z. Y. Qi, Q. Zheng, Y. H. Lu, J. Y. Chen, J. L. Chen, C. W. Pao, S. B. Wang, Y. Bin Li, S. H. Xie, F. D. Liu, D. Prendergast, L. E. Klebanoff, V. Stavila, M. D. Allendorf, J. Guo, L. S. Zheng, J. Su, G. A. Somorjai, Efficient Hydrogen Production from Methanol Using a Single-Site Pt_1/CeO_2 Catalyst. *J. Am. Chem. Soc.* **141**, 17995–17999 (2019).

13. L. Chen, P. Verma, K. Hou, Z. Qi, S. Zhang, Y. Liu, J. Guo, V. Stavila, M. D. Allendorf, L. Zheng, M. Salmeron, D. Prendergast, G. A. Somorjai, J. Su, Reversible dehydrogenation and rehydrogenation of cyclohexane and methylcyclohexane by single-site platinum catalyst. *Nat. Commun.* **13**, 1092 (2022).

14. F. Maurer, J. Jelic, J. Wang, A. Gänzler, P. Dolcet, C. Wöll, Y. Wang, F. Studt, M. Casapu, J. D. Grunwaldt, Tracking the formation, fate and consequence for catalytic activity of Pt single sites on CeO_2. *Nat. Catal.* **3**, 824–833 (2020).

15. R. Gao, J. Wang, Z. F. Huang, R. Zhang, W. Wang, L. Pan, J. Zhang, W. Zhu, X. Zhang, C. Shi, J. Lim, J. J. Zou, Pt/Fe_2O_3 with Pt–Fe pair sites as a catalyst for oxygen reduction with ultralow Pt loading. *Nat. Energy* **6**, 614–623 (2021).

16. I. Ro, J. Qi, S. Lee, M. Xu, X. Yan, Z. Xie, G. Zakem, A. Morales, J. G. Chen, X. Pan, D. G. Vlachos, S. Caratzoulas, P. Christopher, Bifunctional hydroformylation on heterogeneous $Rh\text{-}WO_x$ pair site catalysts. *Nature* **609**, 287–292 (2022).

17. L. Zeng, K. Cheng, F. Sun, Q. Fan, L. Li, Q. Zhang, Y. Wei, W. Zhou, J. Kang, Q. Zhang, M. Chen, Q. Liu, L. Zhang, J. Huang, J. Cheng, Z. Jiang, G. Fu, Y. Wang, Stable anchoring

of single rhodium atoms by indium in zeolite alkane dehydrogenation catalysts. *Science* **383**, 998–1004 (2024).

18. V. Muravev, A. Parastaev, Y. van den Bosch, B. Ligt, N. Claes, S. Bals, N. Kosinov, E. J. M. Hensen, Size of cerium dioxide support nanocrystals dictates reactivity of highly dispersed palladium catalysts. *Science* **380**, 1174–1179 (2023).

19. J. C. Duchet, D. Guillaume, A. Monnier, C. Dujardin, J. P. Gilson, J. Van Gestel, G. Szabo, P. Nascimento, Isomerization of n-hexane over sulfated zirconia: Influence of hydrogen and platinum. *J. Catal.* **198**, 328–337 (2001).

20. O. Pozdnyakova, D. Teschner, A. Wootsch, J. Kröhnert, B. Steinhauer, H. Sauer, L. Toth, F. C. Jentoft, A. Knop-Gericke, Z. Paál, R. Schlögl, Preferential CO oxidation in hydrogen (PROX) on ceria-supported catalysts, part II: Oxidation states and surface species on Pd/CeO_2 under reaction conditions, suggested reaction mechanism. *J. Catal.* **237**, 17–28 (2006).

21. A. Le Valant, C. Comminges, C. Tisseraud, C. Canaff, L. Pinard, Y. Pouilloux, The Cu-ZnO synergy in methanol synthesis from CO_2, Part 1: Origin of active site explained by experimental studies and a sphere contact quantification model on Cu+ZnO mechanical mixtures. *J. Catal.* **324**, 41–49 (2015).

22. J. C. Frost, Junction effect interactions in methanol synthesis catalysts. *Nature* **334**, 577–580 (1988).

23. B. Wang, L. Zhang, J. Cai, Z. Peng, P. Cheng, X. Li, H. Zhang, F. Yang, Z. Liu, Formation and activity enhancement of surface hydrides by the metal–oxide interface. *Adv. Mater. Interfaces* **8**, 2002169 (2021).

24. W. A. Spieker, J. Liu, X. Hao, J. T. Miller, A. J. Kropf, J. R. Regalbuto, An EXAFS study of the coordination chemistry of hydrogen hexachloroplatinate (IV): 1. Speciation in aqueous solution. *Appl. Catal. A Gen.* **232**, 219–235 (2002).

25. C. W. Neil, X. Wu, D. Kim, H. Jung, Y. Zhu, J. R. Ray, Y. Jun, Arsenite oxyanions affect CeO_2 nanoparticle dissolution and colloidal stability. *Environ. Sci.: Nano* **8**, 233–244 (2021).

26. X. Li, X. I. Pereira-Hernández, Y. Chen, J. Xu, J. Zhao, C. W. Pao, C. Y. Fang, J. Zeng, Y. Wang, B. C. Gates, J. Liu, Functional CeO_x nanoglues for robust atomically dispersed catalysts. *Nature* **611**, 284–288 (2022).

27. A. V. Naumkin, A. Kraut-Vass, S. W. Gaarenstroom, C. J. Powell, NIST X-ray Photoelectron Spectroscopy Database, *Gaithersburg, MD: Measurement Services Division of the National Institute of Standards and Technology (NIST)* (2012). https://dx.doi.org/10.18434/T4T88K.

28. M. Baron, O. Bondarehuk, D. Stacchiola, S. Shaikhutdinov, H. J. Freund, Interaction of gold with cerium oxide supports: $CeO_2(111)$ thin films vs CeO_x nanoparticles. *J. Phys. Chem. C* **113**, 6042–6049 (2009).

29. B. Qiao, A. Wang, X. Yang, L. F. Allard, Z. Jiang, Y. Cui, J. Liu, J. Li, T. Zhang, Single-atom catalysis of CO oxidation using Pt_1/FeO_x. *Nat. Chem.* **3**, 634–641 (2011).

30. J. Bentley, S. R. Gilliss, C. B. Carter, J. F. Al-Sharab, F. Cosandey, I. M. Anderson, P. J. Kotula, Nanoscale EELS analysis of oxides: Composition mapping, valence determination and beam damage. J. Phy Conf. Ser. **26**, 69–72 (2006).

31. Z. Wu, Y. Cheng, F. Tao, L. Daemen, G. S. Foo, L. Nguyen, X. Zhang, A. Beste, A. J. Ramirez-Cuesta, Direct neutron spectroscopy observation of cerium hydride species on a cerium oxide catalyst. *J. Am. Chem. Soc.* **139**, 9721–9727 (2017).

32. S. Cao, Y. Zhao, S. Lee, S. Yang, J. Liu, G. Giannakakis, M. Li, M. Ouyang, D. Wang, E. C. H. Sykes, M. Flytzani-Stephanopoulos, High-loading single Pt atom sites [$Pt\text{-}O(OH)_x$] catalyze the CO PROX reaction with high activity and selectivity at mild conditions. *Sci. Adv.* **6**, eaba3809 (2020).

33. J. Saavedra, T. Whittaker, Z. Chen, C. J. Pursell, R. M. Rioux, B. D. Chandler, Controlling activity and selectivity using water in the Au-catalysed preferential oxidation of CO in H_2. *Nat. Chem.* **8**, 584–589 (2016).

34. C. Megías-Sayago, K. Chakarova, A. Penkova, A. Lolli, S. Ivanova, S. Albonetti, F. Cavani, J. A. Odriozola, Understanding the role of the acid sites in 5-hydroxymethylfurfural oxidation to 2,5-furandicarboxylic acid reaction over gold catalysts: surface investigation on $Ce_xZr_{1-x}O_2$ compounds.. *ACS Catal.* **8**, 11154–11164 (2018).

35. Q. Dai, S. Bai, H. Li, W. Liu, X. Wang, G. Lu, Catalytic total oxidation of 1,2-dichloroethane over highly dispersed vanadia supported on CeO_2 nanobelts. *Appl. Catal. B Environ.* **168–169**, 141–155 (2015).

36. C. Binet, M. Daturi, J. C. Lavalley, IR study of polycrystalline ceria properties in oxidised and reduced states. *Catal. Today* **50**, 207–225 (1999).

37. J. Yang, L. J. Falling, S. Yan, B. Zhang, P. Verma, L. Daemen, Y. Cheng, X. Zhao, S. Zhang, J.-L. Chen, B. Yao, S. Tan, S. Chae, Q. He, S. Nemsak, Z. Wu, D. Prendergast, Y. Guo, J. Liu, M. Salmeron, J. Su, Data for: Formation of hydrided Pt-Ce-H sites in efficient, selective oxidation catalysts. *Zenodo* (2025); https://doi.org/10.5281/zenodo.14954782.

38. J. Wan, W. Chen, C. Jia, L. Zheng, J. Dong, X. Zheng, Y. Wang, W. Yan, C. Chen, Q. Peng, D. Wang, Y. Li, Defect effects on TiO_2 nanosheets: Stabilizing single atomic site Au and promoting catalytic properties. *Adv. Mater.* **30**, 1705369 (2018).

39. L. W. Guo, P. P. Du, X. P. Fu, C. Ma, J. Zeng, R. Si, Y. Y. Huang, C. J. Jia, Y. W. Zhang, C. H. Yan, Contributions of distinct gold species to catalytic reactivity for carbon monoxide oxidation. *Nat. Commun.* **7**, 13481 (2016).

40. A. Ben Yaacov, L. J. Falling, R. Ben David, S. Attia, M. A. Andrés, S. Nemšák, B. Eren, Oxidation and reduction of polycrystalline cerium oxide thin films in hydrogen. *J. Phys. Chem. Lett.* **14**, 7354–7360 (2023).

41. G. M. Bancroft, H. W. Nesbitt, R. Ho, D. M. Shaw, J. S. Tse, M. C. Biesinger, Toward a comprehensive understanding of solid-state core-level XPS linewidths: Experimental and theoretical studies on the Si 2p and O 1s linewidths in silicates. *Phys. Rev. B* **80**, 075405 (2009).

42. G. Kresse, J. Furthmüller, Efficiency of ab-initio total energy calculations for metals and semiconductors using a plane-wave basis set. *Comput. Mater. Sci.* **6**, 15–50 (1996).

43. G. Kresse, J. Furthmüller, Efficient iterative schemes for ab initio total-energy calculations using a plane-wave basis set. *Phys. Rev. B* **54**, 11169–11186 (1996).

44. P. E. Blöchl, O. Jepsen, O. K. Andersen, Improved tetrahedron method for Brilleuin-zone integrations. *Phys. Rev. B* **49**, 16223–16233 (1994).

45. G. Kresse, D. Joubert, From ultrasoft pseudopotentials to the projector augmented-wave method. *Phys. Rev. B* **59**, 1758–1775 (1999).

46. S. Grimme, J. Antony, S. Ehrlich, H. Krieg, A consistent and accurate ab initio parametrization of density functional dispersion correction (DFT-D) for the 94 elements H-Pu. *J. Chem. Phys.* **132**, 154104 (2010).

47. J. P. Perdew, K. Burke, M. Ernzerhof, Generalized gradient approximation made simple. *Phys. Rev. Lett.* **77**, 3865–3868 (1996).

48. V. I. Anisimov, F. Aryasetiawan, A. I. Lichtenstein, First-principles calculations of the electronic structure and spectra of strongly correlated systems: The LDA + U method. *J. Phys. Condens. Matter* **9**, 767–808 (1997).

49. V. I. Anisimov, J. Zaanen, O. K. Andersen, Band theory and Mott insulators: Hubbard U instead of Stoner I. *Phys. Rev. B* **44**, 943–954 (1991).

50. F. Dvořák, M. F. Camellone, A. Tovt, N. D. Tran, F. R. Negreiros, M. Vorokhta, T. Skála, I. Matolínová, J. Mysliveček, V. Matolín, S. Fabris, Creating single-atom Pt-ceria catalysts by surface step decoration. *Nat. Commun.* **7**, 10801 (2016).

51. G. Henkelman;, B. P. Uberuaga;, H. Jónsson, A climbing image nudged elastic band method for finding saddle points and minimum energy paths. *J. Chem. Phys.* **113**, 9901–9904 (2000).

52. M. Nolan, S. Grigoleit, D. C. Sayle, S. C. Parker, G. W. Watson, Density functional theory studies of the structure and electronic structure of pure and defective low index surfaces of ceria. *Sur. Sci.* **576**, 217–229 (2005).

53. M. M. Branda, R. M. Ferullo, M. Causá, F. Illas, Relative stabilities of low index and stepped CeO_2 surfaces from hybrid and GGA + U implementations of density functional theory. *J. Phys. Chem. C* **115**, 3716–3721 (2011).

54. N. Daelman, M. Capdevila-Cortada, N. López, Dynamic charge and oxidation state of Pt/CeO_2 single-atom catalysts. *Nat. Mater.* **18**, 1215–1221 (2019).

55. M. M. Kauppinen, N. Daelman, N. López, K. Honkala, The role of polaronic states in the enhancement of CO oxidation by single-atom Pt/CeO_2. *J. Catal.* **423**, 26–33 (2023).

56. G. Kresse, J. Hafner, Ab initio molecular dynamics for open-shell transition metals. *Phy. Rev. B* **48**, 13115–13118 (1993).

57. A. Cimino, F. S. Stone, Oxide solid solutions as catalysts. *Adv. Catal.* **47**, 141–306 (2002).

58. E. W. McFarland, H. Metiu, Catalysis by doped oxides. *Chem. Rev.* **113**, 4391–4427 (2013).

59. W. Yang, F. Qi, W. An, H. Yu, S. Liu, P. Ma, R. Chen, S. Liu, L. L. Lou, K. Yu, Local electronic structure modulation of interfacial oxygen vacancies promotes the oxygen activation capacity of Pt/$Ce_{1-x}M_xO_{2-\delta}$. *ACS Catal.* **14**, 5936–5948 (2024).

60. D. Leybo, U. J. Etim, M. Monai, S. R. Bare, Z. Zhong, C. Vogt, Metal-support interactions in metal oxide-supported atomic, cluster, and nanoparticle catalysis. *Chem. Soc. Rev.* **53**, 10450–10490 (2024).

61. Y. Li, M. Kottwitz, J. L. Vincent, M. J. Enright, Z. Liu, L. Zhang, J. Huang, S. D. Senanayake, W. C. D. Yang, P. A. Crozier, R. G. Nuzzo, A. I. Frenkel, Dynamic structure of active sites in ceria-supported Pt catalysts for the water gas shift reaction. *Nat. Commun.* **12**, 914 (2021).

62. C. Tisseraud, C. Comminges, T. Belin, H. Ahouari, A. Soualah, Y. Pouilloux, A. Le Valant, The Cu-ZnO synergy in methanol synthesis from CO_2, Part 2: Origin of the methanol and CO selectivities explained by experimental studies and a sphere contact quantification model in randomly packed binary mixtures on Cu-ZnO coprecipitate catalysts. *J. Catal.* **330**, 533–544 (2015).

63. W. Tan, S. Xie, D. Le, W. Diao, M. Wang, K. Bin Low, D. Austin, S. Hong, F. Gao, L. Dong, L. Ma, S. N. Ehrlich, T. S. Rahman, F. Liu, Fine-tuned local coordination environment of Pt single atoms on ceria controls catalytic reactivity. *Nat. Commun.* **13**, 7070 (2022).

64. J. H. Carter, X. Liu, Q. He, S. Althahban, E. Nowicka, S. J. Freakley, L. Niu, D. J. Morgan, Y. Li, J. W. H. Niemantsverdriet, S. Golunski, C. J. Kiely, G. J. Hutchings, Activation and deactivation of gold/ceria–zirconia in the low-temperature water–gas shift reaction. *Angew. Chem. Int. Ed.* **56**, 16037–16041 (2017).

65. Y. Lou, L. Wang, Z. Zhao, Y. Zhang, Z. Zhang, G. Lu, Y. Guo, Y. Guo, Low-temperature CO oxidation over Co_3O_4-based catalysts: Significant promoting effect of Bi_2O_3 on Co_3O_4 catalyst. *Appl. Catal. B Environ.* **146**, 43–49 (2014).

66. Y. Yu, T. Takei, H. Ohashi, H. He, X. Zhang, M. Haruta, Pretreatments of Co_3O_4 at moderate temperature for CO oxidation at -80 °C. *J. Catal.* **267**, 121–128 (2009).

67. X. Xie, Y. Li, Z. Liu, M. Haruta, W. Shen, Low-temperature oxidation of CO catalysed by Co_3O_4 nanorods. *Nature* **458**, 746–749 (2009).

68. H. F. Wang, R. Kavanagh, Y. L. Guo, Y. Guo, G. Z. Lu, P. Hu, Structural origin: Water deactivates metal oxides to CO oxidation and promotes low-temperature CO oxidation with metals. *Angew. Chem. Int. Ed.* **51**, 6657–6661 (2012).

69. M. Daté, M. Okumura, S. Tsubota, M. Haruta, Vital role of moisture in the catalytic activity of supported gold nanoparticles. *Angew. Chem. Int. Ed.* **43**, 2129–2132 (2004).

70. M. Comotti, W. C. Li, B. Spliethoff, F. Schüth, Support effect in high activity gold catalysts for CO oxidation. *J. Am. Chem. Soc.* **128**, 917–924 (2006).

71. J. Gong, Structure and surface chemistry of gold-based model catalysts. *Chem. Rev.* **112**, 2987–3054 (2012).

72. B. K. Min, C. M. Friend, Heterogeneous gold-based catalysis for green chemistry: Low-temperature CO oxidation and propene oxidation. *Chem. Rev.* **107**, 2709–2724 (2007).

73. J. Gong, C. B. Mullins, Surface science investigations of oxidative chemistry on gold. *Acc. Chem. Res.* **42**, 1063–1073 (2009).

74. A. A. Herzing, C. J. Kiely, A. F. Carley, P. Landon, G. J. Hutchings, Identification of active gold nanoclusters on iron oxide supports for CO oxidation. *Science* **321**, 1331–1335 (2008).

75. M. Kipnis, Gold in CO oxidation and PROX: The role of reaction exothermicity and nanometer-scale particle size. *Appl. Catal. B Environ.* **152**–**153**, 38–45 (2014).

76. X. Ye, H. Wang, Y. Lin, X. Liu, L. Cao, J. Gu, J. Lu, Insight of the stability and activity of platinum single atoms on ceria. *Nano Res.* **12**, 1401–1409 (2019).

77. D. Kunwar, S. Zhou, A. Delariva, E. J. Peterson, H. Xiong, X. I. Pereira-Hernández, S. C. Purdy, R. Ter Veen, H. H. Brongersma, J. T. Miller, H. Hashiguchi, L. Kovarik, S. Lin, H. Guo, Y. Wang, A. K. Datye, Stabilizing high metal loadings of thermally stable platinum single atoms on an industrial catalyst support. *ACS Catal.* **9**, 3978–3990 (2019).

78. J. Resasco, L. Derita, S. Dai, J. P. Chada, M. Xu, X. Yan, J. Finzel, S. Hanukovich, A. S. Hoffman, G. W. Graham, S. R. Bare, X. Pan, P. Christopher, Uniformity is key in defining structure-function relationships for atomically dispersed metal catalysts: The case of Pt/CeO_2. *J. Am. Chem. Soc.* **142**, 169–184 (2020).

79. Y. Lou, Y. Cai, W. Hu, L. Wang, Q. Dai, W. Zhan, Y. Guo, P. Hu, X. M. Cao, J. Liu, Y. Guo, Identification of active area as active center for CO oxidation over single Au atom catalyst. *ACS Catal.* **10**, 6094–6101 (2020).

80. R. Liu, N. Gao, F. Zhen, Y. Zhang, L. Mei, X. Zeng, Doping effect of Al_2O_3 and CeO_2 on Fe_2O_3 support for gold catalyst in CO oxidation at low-temperature. *Chem. Eng. J.* **225**, 245–253 (2013).

Acknowledgments:

Funding:

The Director, Office of Science, Office of Basic Energy Sciences, Chemical Sciences, Geosciences, and Biosciences Division, of the U.S. Department of Energy under Contract DE-AC02-05CH11231, FWP CH030201 (Catalysis Research Program)

Work by J.Y., L.J.F, and X.Z. was performed as part of a User Project at the Molecular Foundry of the Lawrence Berkeley National Laboratory under Contract No. DE-AC02-05CH11231.

L.J.F acknowledges the support from the Alexander von Humboldt Foundation, Bonn, Germany.

Z.W. was supported by the U.S. Department of Energy, Office of Science, Office of Basic Energy Sciences, Chemical Sciences, Geosciences, and Biosciences Division, Catalysis Science program.

This research used resources of the Advanced Light Source, which is a DOE Office of Science User Facility under Contract No. DE-AC02-05CH11231.

The X-ray absorption near edge structure (XANES) work was supported by National Science and Technology Council of Taiwan under grant NSTC 113-2112-M-213-008.

B.Y. and Q.H. would like to acknowledge the support from Singapore National Research Foundation under Award no. NRF-NRFF11-2019-0002 and Singapore Low-Carbon Energy Research Funding Initiative hosted under A*STAR (Award Nos.: U2102d2006; U2305d4003).

This research used resources of the National Energy Research Scientific Computing Center, which is supported by the Office of Science of the U.S. Department of Energy under Contract No. DE-AC02-05CH11231.

This research used the Lawrencium computational cluster resource provided by the IT Division at the Lawrence Berkeley National Laboratory (Supported by the Director, Office of Science, Office of Basic Energy Sciences, of the U.S. Department of Energy under Contract No. DE-AC02-05CH11231).

This research used resources at the Spallation Neutron Source, a DOE Office of Science User Facility operated by the Oak Ridge National Laboratory.

Author contributions:

Conceptualization: JY, MS, JS

Methodology: JY, LJF, DP, YG, JL, MS, JS

Investigation: JY, LJF, SY, BZ, PV, LD, YC, ZW, XZ, SZ, SC, JLC, BY, ST, QH, SN

Visualization: JY, LJF, SY, BZ, PV, LD, BY

Funding acquisition: MS, JS, DP, LJF, ZW, QH, BY

Project administration: JY, MS, JS

Supervision: JS, MS, JL, YG, DP

Writing – original draft: JY, LJF, SY, BZ, PV

Writing – review & editing: JS, MS, JL, YG, DP, ZW

Competing interests: Authors declare that they have no competing interests.

Data and materials availability: All data are available in the main text or the supplementary materials, including data S1 to S11, or has been deposited at Zenodo (*37*).

Supplementary Materials

Materials and Methods

Supplementary Text

Figs. S1 to S32

Tables S1 to S6

References (*38*-*80*)

Data S1 to S11

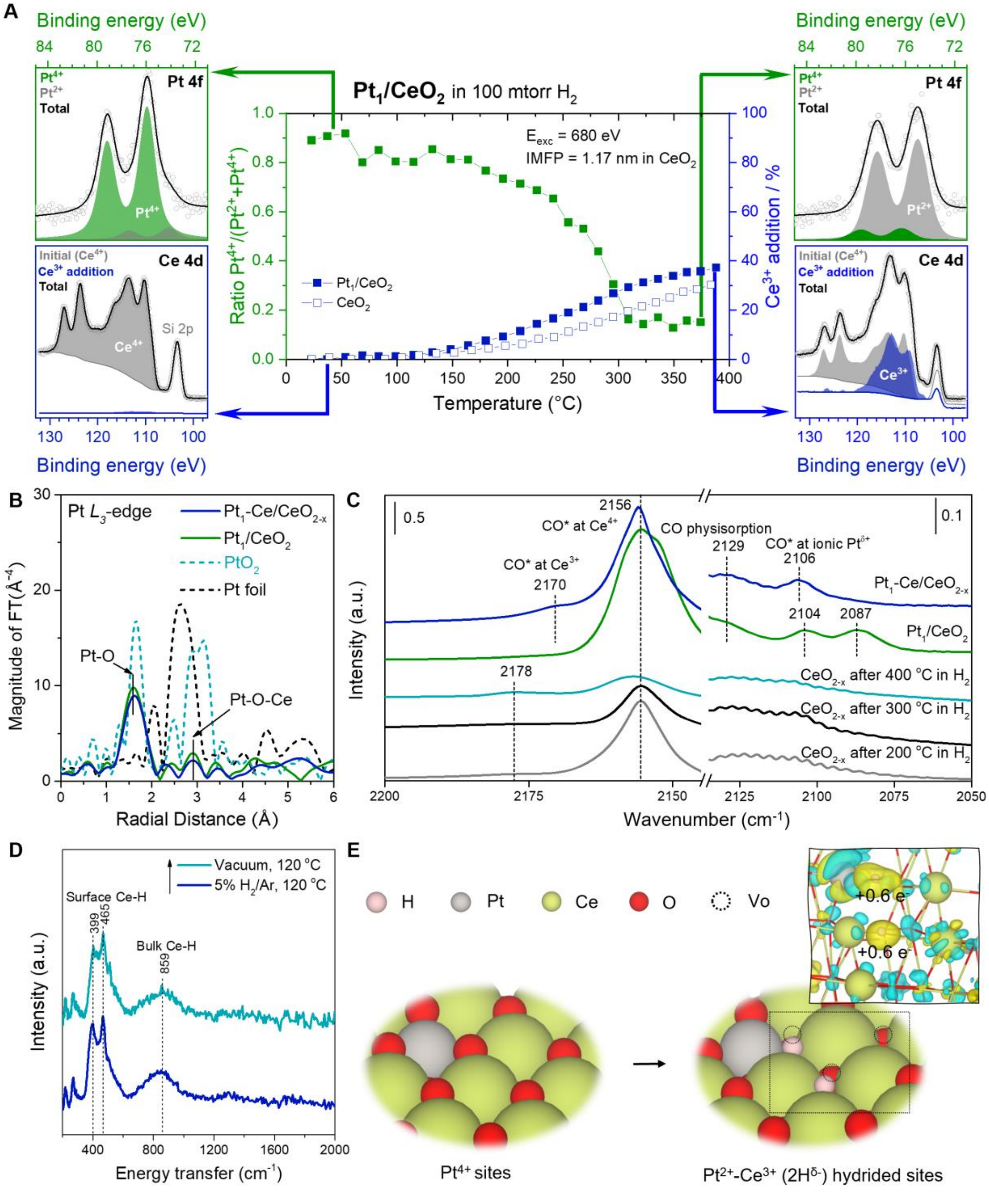

Fig. 1. Formation and structure of hydrided sites Pt^{2+}-Ce^{3+}($H^{\delta-}$). (**A**) APXPS results showing the changes in Pt 4*f* and Ce 4*d* core levels binding energy during formation of the hydrided sites by reaction with H_2 as a function of temperature (middle panel). (**B**) FT-EXAFS spectra of the Pt L_3-edge for Pt_1/CeO_2 and Pt_1-Ce/CeO_{2-x} with reference spectra from Pt foil and PtO_2. (**C**) Dual-beam FTIR spectra at liquid N_2 temperature (77 K) from CO adsorption on Pt_1/CeO_2, Pt_1-Ce/CeO_{2-x} and CeO_{2-x} control samples. (**D**) In-situ INS spectra of Pt_1-Ce/CeO_{2-x} collected at 5K with a purge of 5% H_2/Ar at 120 °C, followed by evacuation at 120 °C. (**E**) DFT models of Pt single sites and hydrided sites Pt^{2+}-Ce^{3+}($H^{\delta-}$), where electron accumulation and depletion are represented by yellow ($\Delta\rho = +1 \times 10^{-3}$ e bohr^{-3}) and cyan ($\Delta\rho = -1 \times 10^{-3}$ e bohr^{-3}) color, respectively.

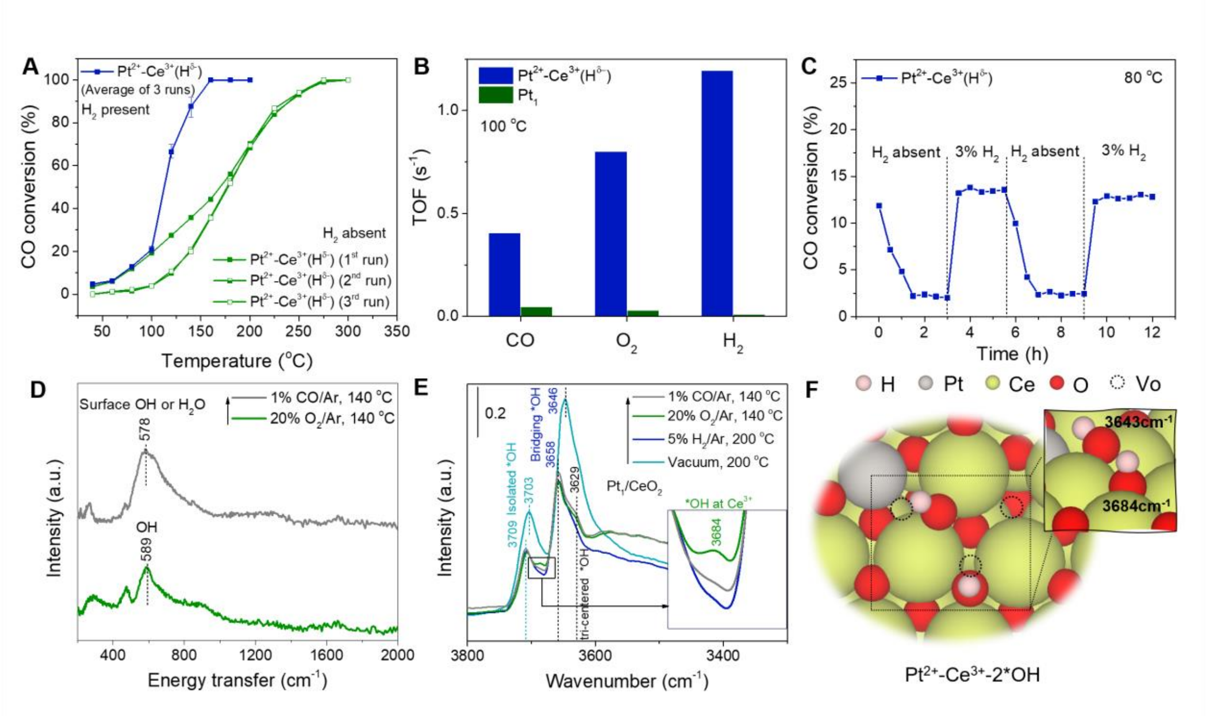

Fig. 2. Catalytic performance of Pt^{2+}-Ce^{3+}($H^{\delta-}$) hydrided-site catalyst and enhanced O_2 activation. (**A**) CO conversion as a function of temperature for Pt^{2+}-Ce^{3+}($H^{\delta-}$) hydrided-site catalyst in the absence and in the presence of H_2 gas. Reaction conditions in the absence of H_2 (H_2 absent): 1% CO + 20% O_2 balanced with argon at weight hourly space velocity (WHSV) of 36,000 mL g^{-1} h^{-1}; Reaction conditions in the presence of 3% H_2 (H_2 present): 1% CO + 20% O_2 + 3% H_2 balanced with argon at WHSV of 36,000 mL g^{-1} h^{-1}; (**B**) Pt site-specific TOF of CO, O_2 and H_2 at 100 °C for Pt^{2+}-Ce^{3+}($H^{\delta-}$) hydrided sites and Pt_1 single sites when 3% H_2 was co-fed; (**C**) Effect of H_2 addition on CO conversion for Pt^{2+}-Ce^{3+}($H^{\delta-}$) hydrided-site catalyst; (**D**) In-situ INS spectra of Pt^{2+}-Ce^{3+}($H^{\delta-}$) hydrided sites collected at 5K with a purge of 20% O_2/Ar at 140 °C, followed by 1% CO/Ar at 140 °C; (**E**) In-situ dual-beam FTIR spectra of surface OH adsorption on Pt single sites followed by evacuation at 200 °C, 5% H_2/Ar at 200 °C, 20% O_2/Ar at 140 °C, and 1% CO/Ar at 140 °C in sequence; (**F**) DFT simulations of O_2 speciation on Pt^{2+}-Ce^{3+}($H^{\delta-}$) hydrided sites.

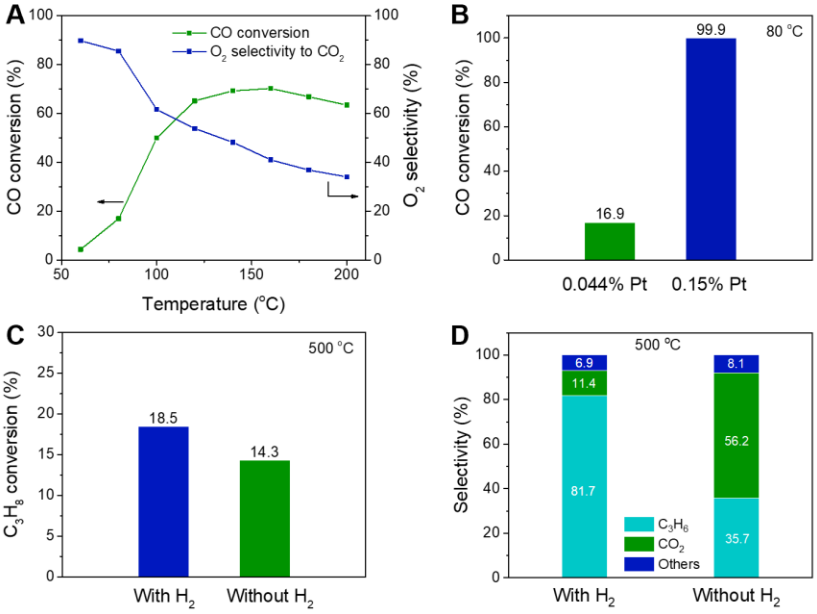

Fig. 3. Expanding the application of Pt^{2+}-Ce^{3+}($H^{\delta-}$) hydrided-site catalysts to other reactions. (**A**) Activity and selectivity for CO to CO_2 conversion during CO preferential oxidation (PROX) by Pt^{2+}-Ce^{3+}($H^{\delta-}$) hydrided-site catalyst. Reaction conditions: 1% CO + 1% O_2 + 40% H_2 balanced with argon at WHSV of 36,000 mL g^{-1} h^{-1}. (**B**) Comparison of CO conversion rate under CO PROX conditions of 1% CO + 1% O_2 + 40% H_2 balanced with argon, for two Pt loadings of 0.044% and 0.15%, tested at WHSV of 36,000 and 12,000 mL g^{-1} h^{-1}, respectively. (**C**) Propane (C_3H_8) conversion rate, and (**D**) product selectivity for oxidative dehydrogenation of propane over Pt^{2+}-Ce^{3+}($H^{\delta-}$) hydrided-site catalysts with/without the participation of H_2. Reaction conditions with H_2 co-feeding: 20% C_3H_8 + 10% O_2 + 20% H_2 + 10% N_2 balanced with helium at WHSV of 24,000 mL g^{-1} h^{-1}; Reaction conditions without H_2: 20% C_3H_8 + 10% O_2 + 10% N_2 balanced with helium at WHSV of 24,000 mL g^{-1} h^{-1}.

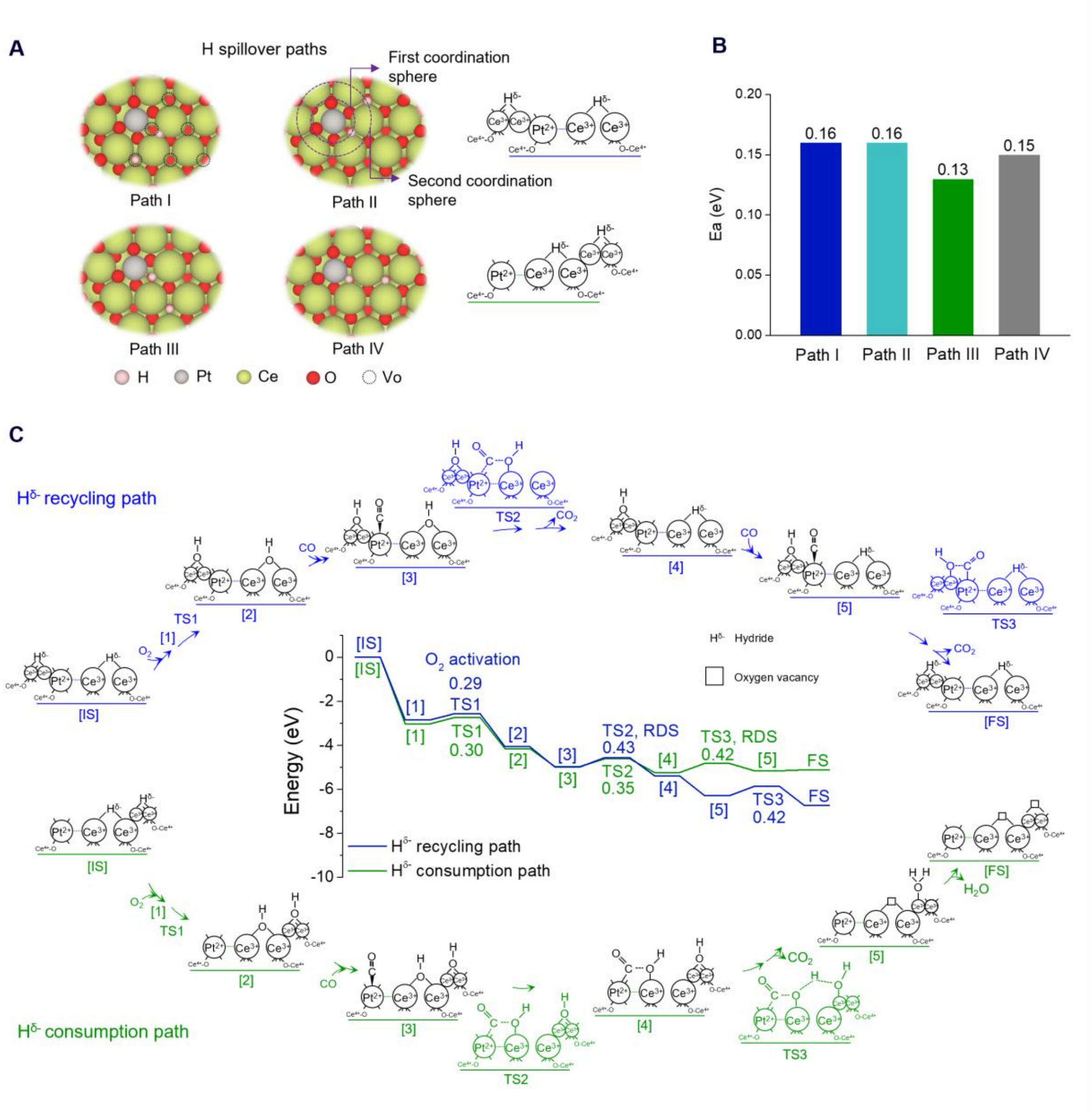

Fig 4. Hydride transfer-controlled CO oxidation mechanism. (**A**) The hydrogen (H) spillover paths on Pt_1-Ce/CeO_{2-x}_6Vo model after H_2 activation; (**B**) Comparison of calculated energy barrier for four H_2 activation paths; (**C**) Catalytic cycles and potential energy diagram of $H^{\delta-}$-transfer enhanced CO oxidation on Pt^{2+}-Ce^{3+}($H^{\delta-}$) hydrided sites. IS, TS and FS represent initial state, transition state, and final state, respectively.